

Contact behavior of a fluttering flag with an adjacent plate

Cite as: Phys. Fluids **33**, 034105 (2021); <https://doi.org/10.1063/5.0037049>

Submitted: 10 November 2020 . Accepted: 27 January 2021 . Published Online: 05 March 2021

 Jeongsu Lee (이정수),  Daegyoun Kim (김대겸), and  Ho-Young Kim (김호영)



View Online



Export Citation



CrossMark

ARTICLES YOU MAY BE INTERESTED IN

[Dispersion of evaporating cough droplets in tropical outdoor environment](#)

Physics of Fluids **32**, 113301 (2020); <https://doi.org/10.1063/5.0026360>

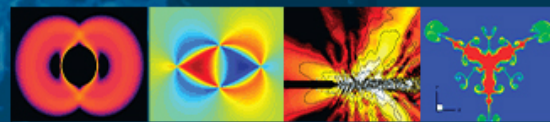
[Effects of time-varying flexibility on the propulsion performance of a flapping foil](#)

Physics of Fluids **32**, 121904 (2020); <https://doi.org/10.1063/5.0027927>

[Collective locomotion of two uncoordinated undulatory self-propelled foils](#)

Physics of Fluids **33**, 011904 (2021); <https://doi.org/10.1063/5.0036231>

Physics of Fluids
GALLERY OF COVERS



Contact behavior of a fluttering flag with an adjacent plate

Cite as: Phys. Fluids **33**, 034105 (2021); doi: [10.1063/5.0037049](https://doi.org/10.1063/5.0037049)

Submitted: 10 November 2020 · Accepted: 27 January 2021 ·

Published Online: 5 March 2021



View Online



Export Citation



CrossMark

Jeongsu Lee (이정수),¹ Daegyoun Kim (김대겸),² and Ho-Young Kim (김호영)^{3,a)}

AFFILIATIONS

¹Intelligent Manufacturing R&D Department, Korea Institute of Industrial Technology, Gyeonggi-do 15014, South Korea

²Department of Mechanical Engineering, KAIST, Daejeon 34141, South Korea

³Department of Mechanical Engineering, Seoul National University, Seoul 08826, South Korea

^{a)}Author to whom correspondence should be addressed: hyk@snu.ac.kr

ABSTRACT

A flag fluttering near a plate exhibits diverse contact behaviors depending on physical conditions such as material and dimensions of the flag and incident air velocity. Here we experimentally investigate the dynamic interactions of the fluttering flag and the plate, combining high-speed imaging and triboelectric sensing. We find that the stability criteria of the flag are identical to those of the isolated flag for an insignificant boundary layer thickness compared with the flag-plate distance. The flag-plate contact modes are classified as tapping, regular clapping, weakly chaotic clapping, and fully chaotic contact modes. We build a regime map to predict the contact modes based on the mass ratio of the fluid to the flag and the velocity ratio of the fluid to the bending wave. Despite contact with the plate, key parameters identifying the characteristics of fluttering of the flutter, such as the reduced frequency (the ratio of the time scale of fluid flow passing through the flag to the period of oscillation) and the Strouhal number (the speed ratio of the flag edge to the wind), are found to be hardly altered compared to those of isolated flags. This indicates that the flag-fluid interaction still plays a dominant role in the fluttering dynamics of the flag adjacent to a plate. Results of this study can serve as a guide in the design of flutter-induced energy harvesting systems and help the biomechanical understanding of the vocal organs of mammals and birds.

Published under license by AIP Publishing. <https://doi.org/10.1063/5.0037049>

I. INTRODUCTION

Early study on the fluttering instability dates back to the seminal work of Rayleigh,¹ which showed that the interface between two moving fluids is always unstable. This study has been elaborated to interpret the fluttering instability of a flag by further taking into account factors such as the density of fluid and solid, flexural rigidity, structural damping, finite dimensions, and incident wind velocity.^{2–11} In addition to the flutter of the isolated flag, variants of the flag configurations, including multiple flags,^{12–17} an inverted flag,^{18–20} and a flexible plate near a free surface,²¹ were investigated to complement the existing knowledge on the fluttering flag dynamics, thus far.

Meanwhile, the flow induced flutter adjacent to a wall was studied as a model system for vocal organs, such as the larynx in mammals and the syrinx in birds, focusing on the flutter without contact.^{22,23} The utilization of the fluttering flag in a viscous channel is suggested to enhance the flow-enhanced mixing²⁴ or the heat transfer characteristics.^{25–27} Recently, the flag-plate system was utilized as a novel wind energy harvester, an alternative to conventional wind turbines, based

on contact electrification of the fluttering flag and the plate.²⁸ The outstanding merits of this system, which include low price and noise, structural simplicity, small size, and high electrical performance, have aroused subsequent studies to elaborate the flutter-driven triboelectric wind energy harvester.^{29–33} However, the electrical performance of the system was of major interest rather than the flag-plate contact dynamics.

Therefore, here we aim to obtain fluid dynamic understanding of the flutter-driven contact of the flag and plate focusing on the following two issues: (1) the stability condition and (2) the dynamic modes of the contact. Previous results for the isolated flag could be a starting point of this study, which is briefly reviewed as follows.

First, the physical origin underlying the initiation of the flag flutter has been an important concern for the flag flutter problem. The scaling law for the critical velocity of the flutter, U_c , suggested by Argentina and Mahadevan² gives a crucial insight to this concern. A scaling law was suggested by considering the balance between the frequencies of the lowest elastic bending mode and aerodynamic

oscillations.² It could be reproduced based on the assumption that the flutter occurs when the work done by the fluid flow excites the critical bending energy for the flag flutter as derived in the following.

Considering a flag having the length L and the width w , the work done by the fluid flow can be expressed as a product of the area, Lw , displacement A , and the pressure difference across the flag, Δp . The pressure difference is scaled as $\Delta p \sim \rho U^2 A/L$ using the classical airfoil theory.^{2,34} The bending energy of the flag is scaled as $\int_0^L Dw\kappa^2 dL \sim Dw(A/L^2)^2 L \sim DwA^2/L^3$. Balancing the work done by the fluid and bending energy of the flag, we can obtain the following scaling relation for the critical velocity:

$$U_c \sim \left(\frac{D}{\rho L^3}\right)^{1/2}. \quad (1)$$

This scaling law provides a conceptual interpretation for the origin of the instability of an isolated flag.

Second, several flutter modes are reported for the isolated flag. In terms of dynamic states,^{3,7,12,35} flutter modes are classified as stable-state, periodic flutter, and chaotic flutter. Meanwhile, flutter modes are classified as node-less, one-node, imperfect node, and multiple-node flutter in terms of deformed shapes.³⁶⁻³⁸ The dynamic modes of the flutter were characterized by two nondimensional parameters:^{12,35-38} the mass ratio of the fluid to the flag, $\mu = \rho L/(\rho_p h)$, and the velocity ratio of the fluid to the bending wave, $\hat{U} = UL(\rho_p h/D)^{1/2}$, where ρ and ρ_p are, respectively, the density of fluid and solid, and L and h are, respectively, the length and thickness of the flag, U is the incident velocity, and D is the flexural rigidity of the flag.

In this study, we examine the stability condition of the flag adjacent to a plate in comparison to the isolated flag. Comparisons are made to previously reported experimental results and theoretical models including the scaling law for the isolated flag. Next, the dynamics of the flutter-initiated contacts are examined in terms of the mass ratio and the nondimensional velocity. The modes of the contact dynamics are then classified, the corresponding regime map is constructed, and the physical origin of the contact mode transitions is examined. Last, the dynamic states of the flag-plate contact are described in terms of

such crucial fluid dynamic dimensionless numbers as the reduced frequency and the Strouhal number.

II. EXPERIMENTAL

To observe the dynamics of a flexible flag without deflection by its own weight, we employed a vertical wind tunnel designed to drive the air flow from top to bottom, as shown in Fig. 1. The contraction area ratio of the wind tunnel is 4:1 and the dimensions of the test section are $28.5 \times 24.5 \text{ cm}^2$ in cross section and 45 cm in length. The blockage ratio was kept below 7% for all the experimental conditions. The wind flow was driven by the 5 H.P blower and the wind speed U varied from 2.2 to 21 m/s. The turbulence level of the wind tunnel is less than 0.5%.

As flag materials, we used polyimide films of 125 and 140 μm thickness, polycarbonate films of 100 and 130 μm thickness, and woven fabric (Solueta Siltex) of 80 μm thickness. The length L of the flag was varied from 5 to 16 cm and the width w from 3 to 8 cm. Thus, the bending stiffness of the flag, $D = Eh^3/[12(1 - \nu^2)]$, with E , h , and ν , respectively, being Young's modulus, thickness of the flag and Poisson's ratio of the flag material, ranged from 2.61×10^{-5} to $6.72 \times 10^{-4} \text{ N m}$. The aspect ratio w/L , the mass ratio, $\mu = \rho L/(\rho_p h)$, and the nondimensional velocity (the velocity ratio of the fluid to the bending wave), $\hat{U} = UL(\rho_p h/D)^{1/2}$, ranged from 0.25 to 1, 0.5 to 2.5, and 15 to 150, respectively. The Reynolds number Re_L is defined as $Re_L = UL/\nu$, where ν is the kinematic viscosity of air. In our experiments, the Reynolds number Re_L ranges from 7.7×10^3 to 1.4×10^5 .

The motion of the flag was imaged using a high-speed camera (Photron APX-RS) at the frame rate of 1500 and 3000 s^{-1} . The contact surface of the plate was covered by polytetrafluoroethylene (PTFE) film that has a higher electron affinity than that of the woven fabric. The gap between the flag and the plate was fixed at 15 mm. The instantaneous voltage difference was then induced by contact electrification whenever contact between the woven flag and the plate occurred.³⁹ The voltage signal was measured using an electrometer (Keithley 6514) to detect the contact as shown in Fig. 1(d).

A useful way to describe the flag flutter dynamics is to analyze the modal behavior from the flag profiles. The x and y positions of the flag profiles are extracted by counting pixels in the high-speed images.

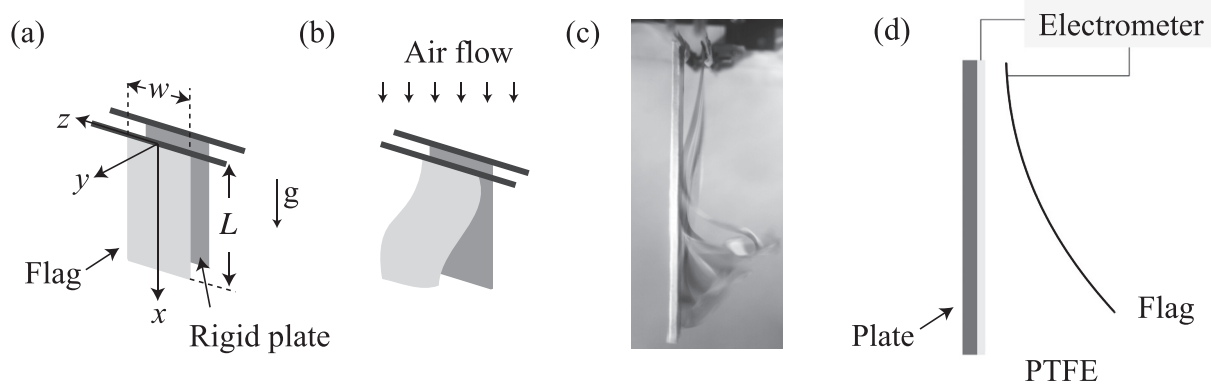


FIG. 1. Schematic diagrams of (a) experimental setup with a flag and a plate situated in parallel and (b) a fluttering flag due to air flow with a velocity over the critical value. (c) Overlapped images of a fluttering woven flag with length $L = 12 \text{ cm}$, width $w = 6 \text{ cm}$, and thickness $h = 80 \mu\text{m}$ under the air flow of $U = 7.3 \text{ m s}^{-1}$. (d) Schematic diagram of the setup to measure the voltage induced at the plate.

We use proper orthogonal decomposition (POD)⁴⁰ and dynamic mode decomposition (DMD)⁴¹ with the displacement data represented in the curvilinear coordinate. The displacement dataset is defined as $\{d_1, d_2, \dots, d_n\}$, where $d_i \in \mathbb{R}^m$, n and m are the number of the displacement data and data point in the displacement data, respectively. In this study, m was fixed at 101 and n varied from 21 to 40 for different fluttering frequencies.

For the POD analysis, the orthonormal basis, $\psi_i \in \mathbb{R}^m$, can be calculated by the eigenvalue decomposition of matrix $\mathbf{Y}^T \mathbf{Y}$, where $\mathbf{Y} = [d_1, d_2, \dots, d_n] \in \mathbb{R}^{m \times n}$,

$$\mathbf{Y}^T \mathbf{Y} q_i = \sigma_i^2 q_i, \tag{2}$$

$$\psi_i = \frac{q_i}{\sigma_i} \mathbf{Y}. \tag{3}$$

Here, σ_i^2 and q_i are the non-zero eigenvalue and the eigenvector of $\mathbf{Y}^T \mathbf{Y}$, respectively. The orthonormal bases satisfy the following expression:⁴⁰

$$\sum_{j=1}^n \left\| d_j - \sum_{i=1}^l (d_j^T \psi_i) \psi_i \right\|^2 \rightarrow \text{minimize}, \tag{4}$$

where l is the number of orthonormal bases. The energy fraction captured by each mode can be calculated as

$$\text{Energy fraction of mode } i = \frac{\sigma_i^2}{\sum_{j=1}^l \sigma_j^2}. \tag{5}$$

The DMD tries to find an optimal linear mapping matrix \mathbf{A} describing the temporal evolution of the system which satisfies the following expression:

$$\sum_{i=1}^{n-1} \|d_{j+1} - \mathbf{A}d_j\|^2 \rightarrow \text{minimize}. \tag{6}$$

This equation can be rewritten in the matrix formulation as

$$\mathbf{V}_2^n \approx \mathbf{A} \mathbf{V}_1^{n-1}, \tag{7}$$

where $\mathbf{V}_i^j = [d_i, d_{i+1}, \dots, d_j]$ for $j > i$. Using a singular value decomposition of the matrix $\mathbf{V}_1^{n-1} = \mathbf{U} \mathbf{\Sigma} \mathbf{W}^T$, we can obtain the following expression from Eq. (7):

$$\tilde{\mathbf{S}} \equiv \mathbf{U}^T \mathbf{A} \mathbf{U} = \mathbf{U}^T \mathbf{V}_2^n \mathbf{W} \mathbf{\Sigma}^{-1}. \tag{8}$$

Then, the eigenvalue λ_A and eigenvector ϕ_A of matrix \mathbf{A} can be calculated from those of the matrix $\tilde{\mathbf{S}}$, $\lambda_A = \lambda_{\tilde{\mathbf{S}}}$ and $\phi_A = \mathbf{U} \phi_{\tilde{\mathbf{S}}}$.

III. RESULTS AND DISCUSSION

A. Stability condition

A flag that is subjected to an incoming flow of fluid begins to flutter when the flow velocity exceeds a critical value that depends on the physical properties of the flag and that of the fluid. The flag can touch an adjacent plate only when the flag flutters a significant amplitude, and thus, investigating the stability condition of the flag is a natural starting point of the current work. We measured the critical fluid velocity inducing the flag flutter by increasing the velocity. We also decreased the fluid velocity after inducing a fluttering motion to measure the velocity at which the flutter stops. Hysteresis was observed for

the critical condition. When the flow velocity decreased, the flag flutter continued far below the critical velocity of flutter onset by increasing the flow velocity. Our primary interest here lies in checking whether any significant difference can be found from the stability condition of the isolated flags.

We plot in Fig. 2 the experimental data in a two-dimensional space constructed by the dimensionless parameters known to critically affect the stability condition, the mass ratio μ , and the ratio of the non-dimensional velocity \hat{U} to μ , together with previously reported experimental data and theoretical predictions for isolated flags.^{47–50} Using this parameter space, we obtain the following two merits.³ First, the plot allows us to examine the most physically intuitive relationship between the flag length L and the wind velocity U when the fluid density and physical properties of the flags are given, $\mu = [\rho / (\rho_p h)] L$ and $\mu / \hat{U} = [(\rho_p h)^{3/2} / (\rho D^{1/2})] U$. Second, the plot reveals the qualitative transition of the flutter behaviors, which appears as a sudden jump in the stability boundary around the mass ratio of 1.2. The transition of flutter behaviors is not clearly observed when it is plotted according to \hat{U} instead of \hat{U} / μ .

Overall, our experimental data agree with the theoretical predictions and other experimental data for isolated flags, indicating an insignificant role of the adjacent plate. When the flag remains stable in the incoming flow, the boundary layer on the plate is a dominant source to distort the uniform incoming flow. The boundary layer thickness of the plate, δ , reaches the most at about 1/5 of the flag-plate gap according to the calculation based on the laminar boundary layer theory, $\delta \approx 5.0L / \text{Re}_L^{1/2}$. The largest Reynolds number in the stable condition is about 1.4×10^5 , which is below the transition Re to turbulence. It is then reasonable that the stability conditions remain unchanged.

The flag tends to flutter with a small oscillation amplitude exhibiting the first mode of bending for $\mu < 1.2$. In this regime where the linear stability analysis is effective, our experimental results for the flag-plate system are in good agreement with both the experimental data of isolated flags and the scaling law from Argentina and Mahadevan,² i.e., $\hat{U} / \mu = 6.22 \mu^{-3/2}$. Once the flutter becomes vigorous enough to enter a nonlinear regime for $\mu > 1.2$, significant scatters are observed in both the current and existing experimental data. This is mainly attributed to the increased nonlinear effects^{3,5} and

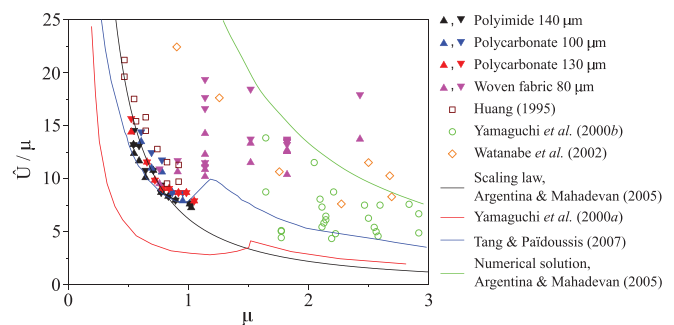


FIG. 2. Plot of critical conditions for flag flutter depending on the mass ratio, μ , and the ratio of the nondimensional velocity to mass ratio. The upright and upside down triangles correspond to the flutter onset condition measured by increasing and decreasing wind velocity, respectively.

planeity defects.⁶ As a result, it is almost impossible to find a single theory to predict the stability boundary.

B. Flag-plate contact modes

Despite insignificant effects of the adjacent wall on the stability condition of the flag, the shape evolution of a flag fluttering near a wall is distinguished from the isolated flags owing to contact with the wall. We observed the flag-plate contact dynamics by varying the wind speed and the flag length while keeping the flag-plate distance at 15 mm, using both the high-speed imaging and triboelectric voltage measurements. We confirmed the reliability of the electrical measurement by checking that the flutter frequency measured from image analysis coincided with the frequency of voltage signals calculated by the FFT (fast Fourier transform) analysis.

As the flag becomes longer and the wind speed increases, the flutter gets more vigorous, so that the flutter regime of an isolated flag evolves from a periodic to a chaotic oscillation. In the presence of the adjacent wall, we found that the flag undergoing mild oscillation just taps the plate with its tip (tapping mode). As the flutter grows stronger, the flag touches the plate with its middle part first and then at the tip in a periodic manner (regular clapping mode). With further strengthening of the flutter, the contact point propagates from the middle to the tip before the flag is completely disengaged from the plate with an unstable trajectory of the tip (weakly chaotic clapping mode). Finally, the flutter becomes fully chaotic resulting in a completely random contact behavior (fully chaotic contact mode). We delineate these contact modes in the following:

1. Tapping mode

Tapping mode refers to when a mildly oscillating flag touches the plate with its tip [Fig. 3(a)]. The resulting voltage signal from the plate

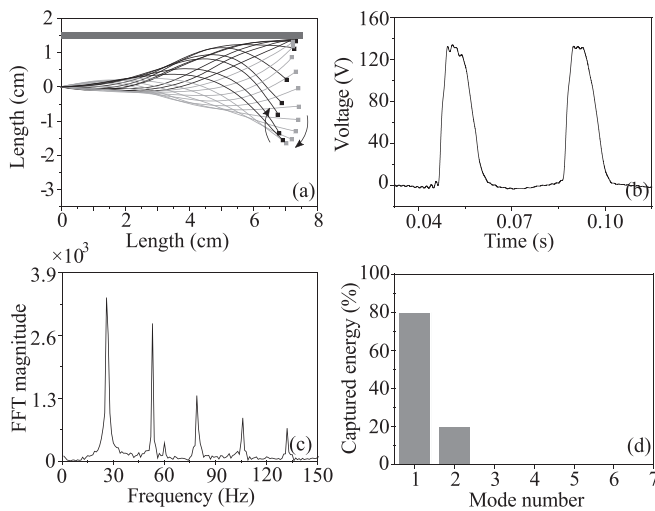


FIG. 3. (a) Overlapped shapes of a flag contacting the plate in the single tapping mode. Here, the mass ratio μ is 1.13, the nondimensional velocity U is 21.5, and the Reynolds number Re_L is 2.8×10^4 . Flags are colored black and gray, before and after touching the wall, respectively. (b) The voltage signal vs time from triboelectrification of the plate. (c) FFT result of the voltage signal. (d) Energy fraction captured by each bending mode.

exhibits regular peaks as shown in Fig. 3(b), whose dominant frequency shown in Fig. 3(c) coincides with the fluttering frequency of the flag obtained from the high-speed images. The modal analysis of the flag reveals that flutter is dominated by the first two bending modes as shown in Fig. 3(d).

2. Regular clapping mode

As the flag gets longer, bending of higher modes arises even at the same wind speed as above. The flag then touches the plate in the middle first and then at the tip as shown in Fig. 4(a). The touch of the middle part inevitably causes contact of a finite area of flag with the plate. Thus, we refer to this mode as the beginning of the clapping mode. Regular contacts by the middle portion and subsequently by the tip are recorded as periodic double peaks of voltage signal in Fig. 4(b). The difference in the adjacent peak voltage values indicates that the areal contact of the middle portion gives rise to greater electricity generation than that of tip tapping. Figure 4(d) reveals slight excitation of the third bending mode. We note that both in the tapping and the regular clapping modes, the flag tip exhibits an asymmetric figure-of-eight trajectory in a periodic manner.

3. Weakly chaotic clapping mode

As the flutter becomes more vigorous, the contact that has begun in the middle is propagated along the flag to the tip [Fig. 5(a)]. This mode is discriminated from the regular clapping mode such that the contact of the middle part propagates along the direction of the traveling wave and that the trajectory of the flag tip is no longer of the regular figure-of-eight shape but becomes irregular and random. The chaotic behavior is confined to the flag tip because the contact point regularly propagates toward the tip. Figure 5(b) shows that the voltage

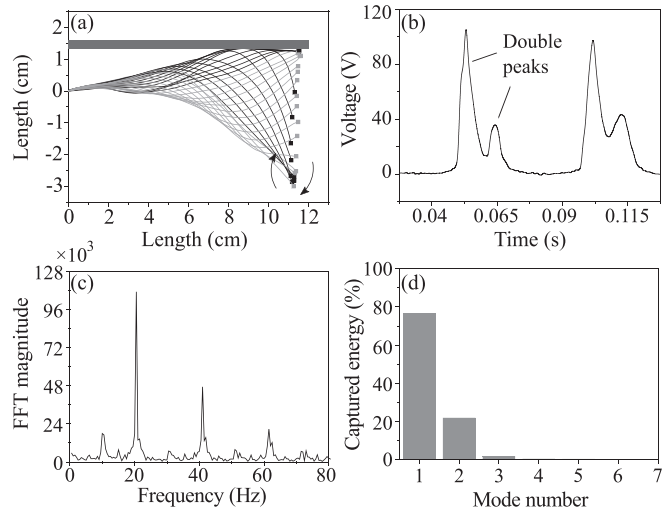


FIG. 4. (a) Overlapped shapes of a flag contacting the plate in the regular clapping mode. Here, the mass ratio μ is 1.82, the nondimensional velocity U is 34.3, and the Reynolds number Re_L is 4.4×10^4 . Flags are colored black and gray, before and after touching the wall, respectively. (b) The voltage signal vs time from triboelectrification of the plate. (c) FFT result of the voltage signal. (d) Energy fraction captured by each bending mode.

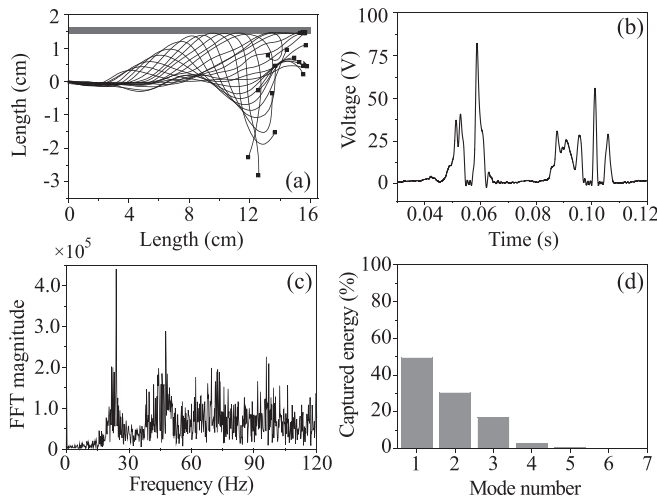


FIG. 5. (a) Overlapped shapes of a flag contacting the plate in a weakly chaotic clapping mode. Here, the mass ratio μ is 2.42, the nondimensional velocity \hat{U} is 64.3, and the Reynolds number Re_L is 8.2×10^4 . (b) The voltage signal vs time from triboelectrification of the plate. (c) FFT result of the voltage signal. (d) Energy fraction captured by each bending mode.

is continuously detected for significantly prolonged duration of the flag-plate contact. The dominant frequency (23 Hz) from the FFT analysis shown in Fig. 5(c) corresponds to the still periodic first contact of the middle of the flag. Modal analysis result in Fig. 5(d) reveals that the third and fourth bending modes are excited to a significant degree.

4. Fully chaotic contact mode

When the flag is under fully chaotic flutter regime, the contact behavior is so random that no rule can be established as shown in Fig. 6(a). It is impossible to predict whether the flag will touch the plate with its tip or middle because it is random. Unlike the foregoing contact regimes, the flag is twisted in a chordwise direction [z-direction in Fig. 1(a)], resulting in an irregular change of the contact area as well. The voltage signals of the fully chaotic mode have much stronger non-periodicity compared to those of the weakly chaotic clapping and thus are quite random with no dominant frequency, resulting in a higher noise of the FFT signal as shown in Fig. 6(c). Bending motions covering from low to high modes are found to arise through the modal analysis presented in Fig. 6(d).

5. Dynamic mode decomposition

We further considered the DMD with the snapshots of the flag profiles in the following. The real and imaginary parts of the DMD eigenvalues represent the dynamic characteristics of the decomposed modes such as growing and decaying,⁴¹ which is presented in Fig. 7 for the contact modes of tapping, regular clapping, weakly chaotic clapping, and fully chaotic contact. DMD eigenvalues show that the transition in the contact modes is closely related to the appearance of additional dynamic modes, corresponding to the results of the POD where the transition in the contact mode promotes excitation of additional bending modes.

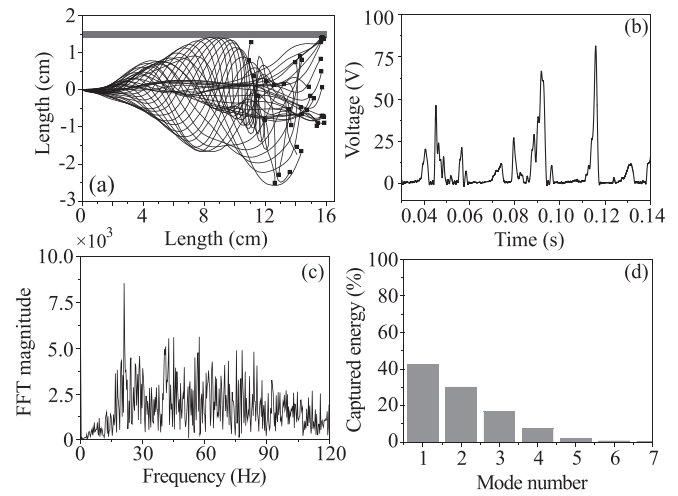


FIG. 6. (a) Overlapped shapes of a flag contacting the plate in a fully chaotic clapping mode. Here, the mass ratio μ is 2.42, the nondimensional velocity \hat{U} is 95.1, and the Reynolds number Re_L is 1.2×10^5 . (b) The voltage signal vs time from triboelectrification of the plate. (c) FFT result of the voltage signal. (d) Energy fraction captured by each bending mode.

For the tapping mode shown in Fig. 7(a), DMD yields two distinct dynamic modes composed of the complex conjugate pairs. The real part of these eigenvalues is negative but close to zero, implying a damped oscillation with a slight decay. Next, the regular clapping mode is accompanied by the appearance of the third mode having a negative real eigenvalue, as shown in Fig. 7(b). This mode corresponds to a non-oscillatory decay. In addition, the two oscillatory modes of the complex conjugate pairs become slightly divergent represented by the positive real part of the eigenvalues close to zero. The fluttering frequency of the tapping and regular clapping mode is solely determined

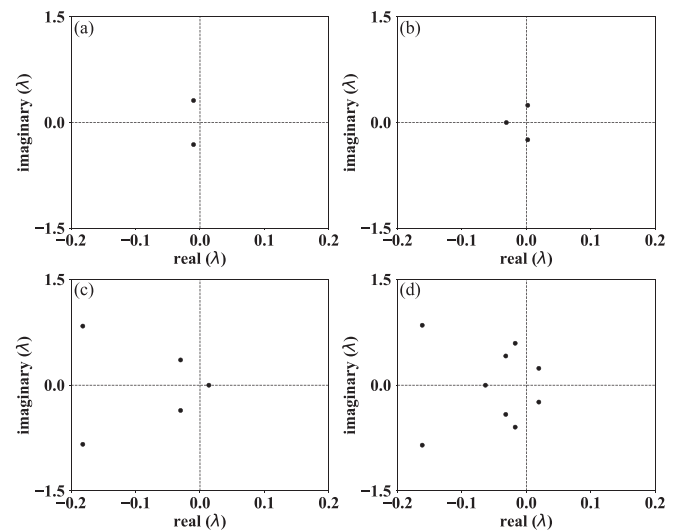


FIG. 7. Eigenvalues obtained from DMD: (a) $\mu = 1.13$, $\hat{U} = 21.5$, (b) $\mu = 1.82$, $\hat{U} = 34.3$, (c) $\mu = 2.42$, $\hat{U} = 64.3$, and (d) $\mu = 2.42$, $\hat{U} = 95.15$.

by the conjugate complex pairs as a definite value corresponding to the periodic flutter of the isolated flag.

The emergence of the chaotic behavior coincides with the excitation of the additional oscillatory mode as shown in Fig. 7(c). The additional oscillatory mode also appears as a complex conjugate pair with a non-integer harmonic frequency. This observation corresponds to the results of the isolated flag where the route to chaos is initiated with the emergence of the non-integer harmonic frequency.^{7,42} Moreover, the divergence of the dynamic modes becomes stronger for the chaotic behavior. For the weakly chaotic clapping mode shown in Fig. 7(c), the non-oscillatory mode becomes divergent having a positive real eigenvalue, while the two oscillatory conjugate pairs are convergent. The transition to fully chaotic modes exhibits the excitation of multiple conjugate pairs, where the primary oscillatory modes diverge as shown in the positive real part of the eigenvalues in Fig. 7(d).

C. Oscillation frequency and amplitude

The symmetry of the flag oscillation is broken due to its interaction with the wall even under mild fluttering. A question naturally arises on whether the frequency and oscillation amplitude of the flag flutter near the plate are different from those of the isolated flags. Figures 8(a) and 8(b) plot our experimental measurement results of the frequency and the amplitude in the positive y axis under interaction with the adjacent plate vs the nondimensional velocity \hat{U} . We measured the frequency and amplitude for each cycle and reported the ranges (maximum to minimum) of observations indicated by the error bars. Here, the amplitude is the maximum distance of the flag tip from the center plane [the zx -plane in Fig. 1(a)] before it begins approaching the plate. The nondimensional velocity was taken as a characteristic measure of the strength of fluid-induced excitation of flag

deformation. The experiments used three different flags with mass ratios of 1.13, 1.82, and 2.42, which exhibit tapping, regular clapping, and weakly chaotic clapping modes around the flutter onset velocity, respectively.

Figure 8(a) shows that the oscillation frequency increases with the nondimensional velocity regardless of the contact modes. The increasing rate of the frequency is highest for the tapping mode because the flag in this mode stores the smallest bending energy compared to the kinetic energy owing to its low bending modes. The flapping amplitude in Fig. 8(b) increases with the nondimensional velocity before the transition to fully chaotic mode at high \hat{U} . In the fully chaotic regime, the flapping amplitude is lower than the maximum exhibited in the weakly chaotic clapping regime. This is attributed to the excitation of a broad range of bending modes in the fully chaotic contact mode. Still, no general rule can be drawn in the fully chaotic mode with the amplitude changing significantly for each flapping cycle.

Based on the experimental observations on the oscillation frequency and amplitude, two nondimensional parameters—the reduced frequency (fL/U) and the Strouhal number ($St = 2fA/U$) describing the interaction characteristics of fluid flow and flag flutter—are obtained as shown in Figs. 8(c) and 8(d), respectively. The reduced frequency is the ratio of the duration of fluid flow passing through the flag (L/U) to the period of oscillation ($1/f$). The reduced frequencies of the three different flags are confined in a narrow range of 0.3 to 0.6 as shown in Fig. 8(c), despite significant changes in fluttering frequency. These results are consistent with previous observations on isolated flag flutter, which show the adjustment of the reduced frequencies toward the similar values from around 0.3 to 0.6 as summarized in Table II. This indicates that the interaction characteristics of fluid and flag flutter are dominated by the inherent properties of the fluttering flag rather than that of the contact. The Strouhal number is

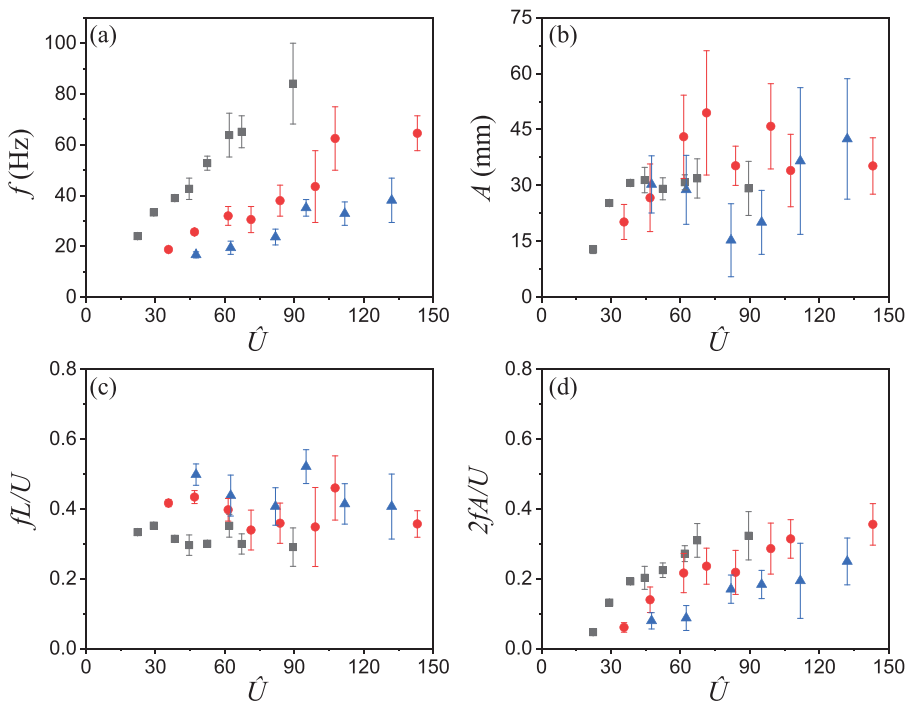


FIG. 8. Frequency and amplitude of flag flutter adjacent to a plate as a function of the nondimensional velocity, \hat{U} . (a) Experimentally measured frequency. (b) Experimentally measured amplitude. (c) The reduced frequency. (d) The Strouhal number. The experimental conditions for each symbol are listed in Table I.

TABLE I. Experimental conditions for the symbols in Fig. 8.

Symbol	Length (cm)	Width (cm)	Thickness (μm)	Density (kg/m^3)	Flexural rigidity (N m)	Mass ratio	Contact mode
■	7.5	5	80	988	2.61×10^{-5}	1.13	Tapping
●	12	8	80	988	2.61×10^{-5}	1.82	Regular clapping
▲	16	10.5	80	988	2.61×10^{-5}	2.42	Weakly chaotic clapping

TABLE II. Reported reduced frequencies of the isolated flag.

Publication	Reduced frequency	Conditions
Eloy <i>et al.</i> (2008) ⁵	0.29–0.59	$\mu = 0.74\text{--}1.94$; $\hat{U} = 8.1\text{--}10.4$
Virot <i>et al.</i> (2013) ³⁷	0.29–0.48	$\mu = 0.69\text{--}2.84$; $\hat{U} = 8.3\text{--}13.5$
Chen <i>et al.</i> (2014) ⁴³	0.35–0.45	$\mu = 1$; $\hat{U} = 0\text{--}20$

TABLE III. Reported Strouhal numbers of the isolated flag.

Publication	Strouhal number
Shelley <i>et al.</i> (2005) ⁴⁴	0.22–0.31
Connell and Yue (2007) ⁷	0.29–0.48
Huang and Sung (2010) ⁸	0.16–0.35

the ratio of the velocity of the flag edge ($2Af$) and the wind speed (U), which describes the interaction dynamics of an object moving in the fluid and wake generated by the motion of the object.⁴⁵ Figure 8(d) shows that the Strouhal number monotonically increases with the nondimensional velocity and tends to converge around 0.2 to 0.4 above the nondimensional velocity of approximately 60, regardless of the mass ratio. This value corresponds to the isolated flag cases

summarized in Table III and the optimal Strouhal number of swimming and flying animals.⁴⁶

Our observations indicate that the flag–fluid interaction has a dominant influence on the fluttering dynamics, despite the contact between the flag and the plate. It is peculiar because the contact between the flag and the plate largely disturbs fluttering behaviors via the instantaneous dissipation of the kinetic energy of the flag. We attribute these findings to the characteristics of the contact behaviors that the momentary impact is restricted to a quarter of the flag regardless of contact modes. Even though the first contact was made around the midpoint of the flag as shown in the weakly chaotic clapping mode, the contact point around the midpoint smoothly swaps along the plate and the last impact occurs around the edge of the flag. This makes the energy transfer of the flag adjacent to the plate similar to that of the isolated flag, resulting in similar values of the reduced frequency and the Strouhal number. The energy is transferred from the fluid to the flag along the middle part of the flag, whereas the mechanical energy of the flag is extracted to the fluid at the tip.³⁸

D. Regime map

We provide a regime map that can predict the contact modes of the flag and plate based on our experimental observations. The map is constructed based on the two most important nondimensional parameters known to affect the flag dynamics, the mass ratio μ , and the ratio of the nondimensional velocity to mass ratio, \hat{U}/μ . The plot in Fig. 9

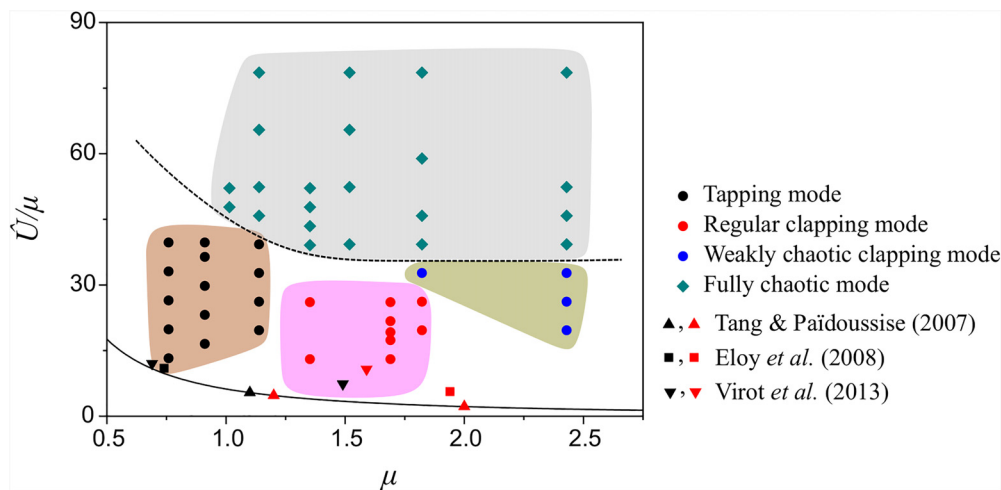


FIG. 9. Regime map of flag-plate contact modes. The black solid line corresponds to the scaling law for the flutter onset condition ($\hat{U}/\mu = 6.22\mu^{-3/2}$) and the broken line refers to the empirical condition for transition to a fully chaotic mode. The reported fluttering modes of the isolated flag in Table IV are incorporated in this plot with red and black colors indicating the single neck and double neck modes, respectively.

TABLE IV. Reported fluttering modes of the isolated flag.

Publication	Fluttering mode	Conditions
Tang and Païdoussis (2007) ³	Single neck	$\mu = 0.2; \hat{U} = 9.95$
		$\mu = 0.2; \hat{U} = 13.78$
	Dobule neck	$\mu = 1.1; \hat{U} = \text{critical condition}$ $\mu = 1.2; \hat{U} = \text{critical condition}$ $\mu = 2.0; \hat{U} = \text{critical condition}$
Eloy <i>et al.</i> (2008) ⁵	Single neck	$\mu = 0.74; \hat{U} = 8.1$
	Doble neck	$\mu = 1.94; \hat{U} = 10.9$
Virot <i>et al.</i> (2013) ³⁷	Single neck	$\mu = 0.69; \hat{U} = 8.3$
		$\mu = 1.49; \hat{U} = 11.0$
	Dobule neck	$\mu = 1.59; \hat{U} = 17.1$ $\mu = 2.84; \hat{U} = 13.5$

has two transition boundaries of the dynamic states: (1) critical condition for flutter above which periodic oscillation arises and (2) transition to a fully chaotic mode. When the flag-plate contact occurs in a periodic manner, contact behaviors can be classified as tapping and clapping modes. Increase in the mass ratio leads to the transition from tapping to clapping mode, which corresponds to the transition of modal behavior of the isolated flag around a mass ratio of 1.2–1.5 reported by previous publications. Transition from the single neck to double neck flutter is summarized in Table IV.

The transition to chaotic mode from the periodic oscillation is less obvious because there is an intermediate weakly chaotic clapping mode that exhibits an irregular behavior in a confined area of the flag tip. The weakly chaotic clapping mode is observed for the mass-ratio above 1.8. Before the mass ratio of approximately 2.4, the transition from weakly chaotic clapping to fully chaotic contact mode is initiated by increasing the wind speed. On the other hand, the flag is highly destabilized above the mass ratio of 2.4, showing the weakly chaotic clapping behavior just above the critical velocity for flutter.

Furthermore, for the mass ratio above approximately 1.3, the transition boundary of \hat{U}/μ is shown to be nearly independent of the mass ratio, thus leading to $\hat{U}/\mu \sim \text{constant}$ with an estimated value around 35. The transition to the fully chaotic mode is relevant to the excitation of the multiple oscillatory modes as shown in Fig. 7(d). We suppose that there is a possible asymptotic limit where the flag is vulnerable to the excitation of multiple dynamic modes resulting in a fully chaotic behavior. It is worth further investigating to see if there exists a similar boundary for the fully chaotic behavior for isolated flags.

IV. CONCLUSIONS

We have experimentally investigated the dynamics of a fluttering flag interacting with an adjacent rigid plate. Of particular interest were the critical conditions to induce flutter, the contact modes of flag and plate, and the frequency and amplitude of oscillation. We have found that the contact mode evolves from regular to chaotic as the flag length and incident fluid velocity increase. In the regular regime, the flag first touches the plate only with its tip (tapping mode). However, it touches the plate with its middle part and then the tip (regular clapping mode) as the flutter becomes more vigorous. Before the contact mode becomes fully chaotic, an intermediate regime appears where the

chaotic behavior is limited to the flag tip, while the periodic contact-propagation occurs from the middle to the tip of the flag.

The physical mechanisms underlying the contact mode transitions were examined based on the POD and DMD. The transition boundary from the tapping to regular clapping contact modes corresponds to the fluttering mode transition of the isolated flag from the single neck to the double neck flutter.^{3,5,37} The emergence of the chaotic behavior is shown to be initiated by the excitation of the additional oscillatory mode with a non-integer harmonic frequency. The same observations are reported in the isolated flag for the route to chaos as well.^{7,41} In addition, the eigenvalues obtained from the DMD suggest that the chaotic behavior can be interpreted by the strong diverging tendency of the dynamic modes composing the fluttering behavior.

Despite such rich interaction dynamics of the flag with the adjacent plate, the critical condition for flutter onset, the reduced frequency, and the Strouhal number have been found to slightly change from that of the isolated flags. The fluttering frequency is almost identical to that of the isolated flag even with a contact, resulting in a similar level of reduced frequency. The fluttering amplitude decreases by the contact near the critical condition. However, it rapidly increases by the wind velocity showing the adjustment of the Strouhal number from 0.3 to 0.6, which corresponds to that of the isolated flag and the reported optimal Strouhal number of the flapping-based locomotion.

The interaction of the flexible flags with rigid plates is recently drawing great interest for its practical applications in triboelectric harvesting of wind energy. The frequency and contact duration determine the electrical power collected by the contact electrification that is converted from the kinetic energy of the flag, which in turn comes from the incident air flow. This work predicts that a longer flag under a stronger wind contacts the plate longer and more frequently, helping us to harvest more energy from the environmental air flow. However, the longer flag stores more elastic bending energy due to the excitation of higher bending modes, resulting in the decrease in the kinetic energy of the flag. Thus, we anticipate that an optimal flag condition exists for wind energy harvesting, a topic awaiting further study.

Different contact modes of flexible flag with adjacent wall have direct implications on how mammals and birds generate sound using their vocal organs consisting of a flexible membrane and a surrounding channel. In particular, the contact of the flexible membrane to the channel is relevant to some failure situations in a vocal organ such as snoring, where the extreme behavior of the fluttering membrane possibly causes the blockage of the airway path.²² Hence, further efforts are encouraged to investigate the relationship between the extreme failure situations in the vocal organ and the fundamental contact modes of a flag and an adjacent wall.

ACKNOWLEDGMENTS

This research was supported by the National Research Foundation of Korea (Grant No. 2018052541) via SNU IAMD.

APPENDIX: EFFECTS OF THE FLAG-PLATE DISTANCE

We observed the fluttering dynamics of a flag adjacent to the plate by changing the flag-plate distance and the incoming velocity as shown in Fig. 10. The fluttering amplitudes of the plate side and

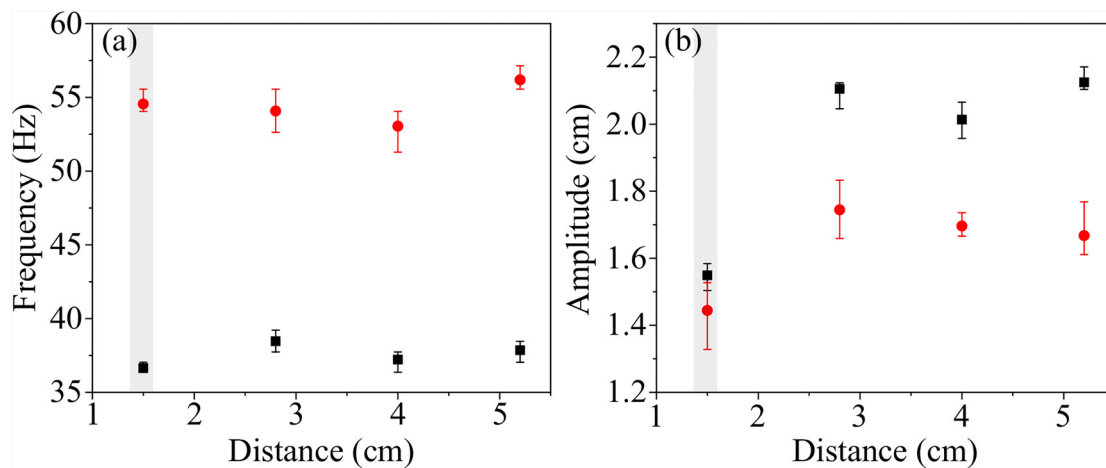


FIG. 10. Fluttering (a) frequency and (b) amplitude for the flag having the mass ratio μ of 0.30. Here, red circles and black rectangles correspond to the nondimensional velocity \hat{U} of 3.9 and 5.2, respectively. Gray bars indicate that the contact between the flag and the plate arises.

the opposite side are almost identical except when the contact of the flag and the plate was made, implying the insignificant influence of the plate on the fluttering dynamics. For the small flag-plate distance, the flag flutter makes a continuous contact with the plate. In this situation, the fluttering frequency remains almost unchanged compared to the case without contact as shown in Fig. 10(a). The fluttering amplitude significantly decreases due to the dissipation of the energy caused by the contact as shown in Fig. 10(b). However, for the flag flutter without the contact, there were no significant changes in the fluttering dynamics including the frequency and the amplitude by the flag-plate distances. The trends in frequency and amplitude largely depend on the incoming wind velocity.

DATA AVAILABILITY

The data that support the findings of this study are available upon request from the authors.

REFERENCES

- 1L. Rayleigh, "On the instability of jets," *Proc. London Math. Soc.* **s1-10**, 4–13 (1878).
- 2M. Argentina and L. Mahadevan, "Fluid-flow-induced flutter of a flag," *Proc. Natl. Acad. Sci. U.S.A.* **102**, 1829–1834 (2005).
- 3L. Tang and M. P. Païdoussis, "On the instability and the post-critical behaviour of two-dimensional cantilevered flexible plates in axial flow," *J. Sound Vib.* **305**, 97–115 (2007).
- 4L. Tang and M. P. Païdoussis, "The influence of the wake on the stability of cantilevered flexible plates in axial flow," *J. Sound Vib.* **310**, 512–526 (2008).
- 5C. Eloy, R. Lagrange, and L. Schouveiler, "Aeroelastic instability of a flexible plate in a uniform flow," *J. Fluid Mech.* **611**, 97–106 (2008).
- 6C. Eloy, N. Kofman, and L. Schouveiler, "The origin of hysteresis in the flag instability," *J. Fluid Mech.* **691**, 583–593 (2012).
- 7B. S. H. Connell and D. K. P. Yue, "Flapping dynamics of a flag in a uniform stream," *J. Fluid Mech.* **581**, 33–67 (2007).
- 8W.-X. Huang and H. J. Sung, "Three-dimensional simulation of a flapping flag in a uniform flow," *J. Fluid Mech.* **653**, 301–336 (2010).
- 9M. A. Langthjem, "On the mechanism of flutter of a flag," *Acta Mech.* **230**, 3759–3781 (2019).
- 10J. Ryu, S. G. Park, W.-X. Huang, and H. J. Sung, "Hydrodynamics of a three-dimensional self-propelled flexible plate," *Phys. Fluids* **31**, 021902 (2019).
- 11Y. Yu, Y. Liu, and X. Amandolese, "A review on fluid-induced flag vibrations," *Appl. Mech. Rev.* **71**, 010801 (2019).
- 12J. Zhang, S. Childress, A. Libchaber, and M. Shelley, "Flexible filaments in a flowing soap film as a model for one-dimensional flags in a two-dimensional wind," *Nature* **408**, 835–839 (2000).
- 13D. J. J. Farnell, T. David, and D. C. Barton, "Coupled states of flapping flags," *J. Fluids Struct.* **19**, 29–36 (2004).
- 14L.-B. Jia, F. Li, X.-Z. Yin, and X.-Y. Yin, "Coupling modes between two flapping filaments," *J. Fluid Mech.* **581**, 199–220 (2007).
- 15L. Ristroph and J. Zhang, "Anomalous hydrodynamic drafting of interacting flapping flags," *Phys. Rev. Lett.* **101**, 194502 (2008).
- 16S. Kim, W.-X. Huang, and H. J. Sung, "Constructive and destructive interaction modes between two tandem flexible flags in viscous flow," *J. Fluid Mech.* **661**, 511–521 (2010).
- 17J. O'Connor and A. Revell, "Dynamic interactions of multiple wall-mounted flexible flaps," *J. Fluid Mech.* **870**, 189–216 (2019).
- 18D. Kim, J. Cossé, C. H. Cerderira, and M. Gharib, "Flapping dynamics of an inverted flag," *J. Fluid Mech.* **736**, R1 (2013).
- 19H. Kim and D. Kim, "Stability and coupled dynamics of three-dimensional dual inverted flags," *J. Fluids Struct.* **84**, 18–35 (2019).
- 20J. W. Park, J. Ryu, and H. J. Sung, "Effects of the shape of an inverted flag on its flapping dynamics," *Phys. Fluids* **31**, 021904 (2019).
- 21J. Mougél and S. Michelin, "Flutter and resonances of a flag near a free surface," *J. Fluids Struct.* **96**, 103046 (2020).
- 22T. S. Balint and A. D. Lucey, "Instability of a cantilevered flexible plate in viscous channel flow," *J. Fluids Struct.* **20**, 893–912 (2005).
- 23J. B. Grotberg and O. E. Jensen, "Biofluid mechanics in flexible tubes," *Annu. Rev. Fluid Mech.* **36**, 121–147 (2004).
- 24A. Rips and R. Mittal, "Flutter-enhanced mixing in small-scale mixers," *Phys. Fluids* **31**, 107107 (2019).
- 25Y. Chen, Y. Yu, W. Zhou, D. Peng, and Y. Liu, "Heat transfer enhancement of turbulent channel flow using tandem self-oscillating inverted flags," *Phys. Fluids* **30**, 075108 (2018).
- 26R. K. B. Gallegos and R. N. Sharma, "Heat transfer performance of flag vortex generators in rectangular channels," *Int. J. Therm. Sci.* **137**, 26–44 (2019).
- 27A. Rips, K. Shoele, and R. Mittal, "Heat transfer enhancement in laminar flow heat exchangers due to flapping flags," *Phys. Fluids* **32**, 063603 (2020).
- 28J. Bae, J. Lee, S. Kim, J. Ha, B.-S. Lee, Y. Park, C. Choong, J.-B. Kim, Z. L. Wang, H.-Y. Kim, J.-J. Park, and U. I. Chung, "Flutter-driven triboelectricification for harvesting wind energy," *Nat. Commun.* **5**, 4929 (2014).
- 29T. Jiang, L. M. Zhang, X. Chen, C. B. Han, W. Tang, C. Zhang, L. Xu, and Z. L. Wang, "Structural optimization of triboelectric nanogenerator for harvesting water wave energy," *ACS Nano* **9**, 12562–12572 (2015).

- ³⁰S. Wang, X. Mu, X. Wang, A. Y. Gu, Z. L. Wang, and Y. Yang, “Elasto-aerodynamics-driven triboelectric nanogenerator for scavenging air-flow energy,” *ACS Nano* **9**, 9554–9563 (2015).
- ³¹L. M. Zhang, C. B. Han, T. Jiang, T. Zhou, X. H. Li, C. Zhang, and Z. L. Wang, “Multilayer wavy-structured robust triboelectric nanogenerator for harvesting water wave energy,” *Nano Energy* **22**, 87–94 (2016).
- ³²Z. Quan, C. B. Han, T. Jiang, and Z. L. Wang, “Robust thin films-based triboelectric nanogenerator arrays for harvesting bidirectional wind energy,” *Adv. Energy Mater.* **6**, 1501799 (2016).
- ³³M. Xu, Y. C. Wang, S. L. Zhang, W. Ding, J. Cheng, X. He, P. Zhang, Z. Wang, X. Pan, and Z. L. Wang, “An aeroelastic flutter based triboelectric nanogenerator as a self-powered active wind speed sensor in harsh environment,” *Extreme Mech. Lett.* **15**, 122–129 (2017).
- ³⁴A. Katz and J. Plotkin, *Low-Speed Aerodynamics, The Art of Computer Programming*, 2nd ed. (Cambridge University Press, 2001).
- ³⁵S. Alben and M. J. Shelley, “Flapping states of a flag in an inviscid fluid: Bistability and the transition to chaos,” *Phys. Rev. Lett.* **100**, 074301 (2008).
- ³⁶S. Taneda, “Waving motions of flags,” *J. Phys. Soc. Jpn.* **24**, 392–401 (1968).
- ³⁷E. Virost, X. Amandolese, and P. Hémon, “Fluttering flags: An experimental study of fluid forces,” *J. Fluids Struct.* **43**, 385–401 (2013).
- ³⁸L. Tang, M. P. Païdoussis, and J. Jiang, “Cantilevered flexible plates in axial flow: Energy transfer and the concept of flutter-mill,” *J. Sound Vib.* **326**, 263–276 (2009).
- ³⁹J. Lowell and A. C. Rose-Innes, “Contact electrification,” *Adv. Phys.* **29**, 947–1023 (1980).
- ⁴⁰G. Berkooz, P. Holmes, and J. L. Lumley, “The proper orthogonal decomposition in the analysis of turbulent flows,” *Annu. Rev. Fluid Mech.* **25**, 539–575 (1993).
- ⁴¹P. J. Schmid, “Dynamic mode decomposition of numerical and experimental data,” *J. Fluid Mech.* **656**, 5–28 (2010).
- ⁴²A. Goza and T. Colonius, “Modal decomposition of fluid–structure interaction with application to flag flapping,” *J. Fluids Struct.* **81**, 728–737 (2018).
- ⁴³M. Chen, L. B. Jia, Y. F. Wu, X. Z. Yin, and Y. B. Ma, “Bifurcation and chaos of a flag in an inviscid flow,” *J. Fluids Struct.* **45**, 124–137 (2014).
- ⁴⁴M. Shelley, N. Vandenberghe, and J. Zhang, “Heavy flags undergo spontaneous oscillations in flowing water,” *Phys. Rev. Lett.* **94**, 094302 (2005).
- ⁴⁵C. H. Williamson, “Vortex dynamics in the cylinder wake,” *Annu. Rev. Fluid Mech.* **28**, 477–539 (1996).
- ⁴⁶G. K. Taylor, R. L. Nudds, and A. L. R. Thomas, “Flying and swimming animals cruise at a strouhal number tuned for high power efficiency,” *Nature* **425**, 707–711 (2003).
- ⁴⁷N. Yamaguchi, K. Yokota, and Y. Tsujimoto, “Flutter limits and behaviors of a flexible thin sheet in high-speed flow. I. Analytical method for prediction of the sheet behavior,” *ASME J. Fluids Eng.* **122**, 65–73 (2000).
- ⁴⁸N. Yamaguchi, T. Sekiguchi, K. Yokota, and Y. Tsujimoto, “Flutter limits and behaviors of a flexible thin sheet in high-speed flow. II. Experimental results and predicted behaviors for low mass ratios,” *ASME J. Fluids Eng.* **122**, 74–83 (2000).
- ⁴⁹L. X. Huang, “Flutter of cantilevered plates in axial flow,” *J. Fluids Struct.* **9**, 127–147 (2000).
- ⁵⁰Y. Watanabe, S. Suzuki, M. Sugihara, and Y. Sueoka, “An experimental study of paper flutter,” *J. Fluids Struct.* **16**, 529–542 (2002).